

Contact effects on thermoelectric properties of textured graphene nanoribbons

David M T Kuo¹ and Yia-Chung Chang^{2,3}

¹*Department of Electrical Engineering and Department of Physics,
National Central University, Chungli, 320 Taiwan*

²*Research Center for Applied Sciences, Academic Sinica, Taipei, 11529 Taiwan and*

³*Department of Physics, National Cheng Kung University, Tainan, 701 Taiwan*

(Dated: September 27, 2022)

Transport and thermoelectric properties of finite textured graphene nanoribbons (t-GNRs) connected to electrodes with various coupling strengths are theoretically studied in the framework of the tight-binding model and Green's function approach. Due to quantum constriction induced by the indented edges, such t-GNRs behave like serially-coupled graphene quantum dots (SGQDs). These types of SGQDs can be formed by tailoring zigzag GNRs (ZGNRs) or armchair GNRs (AGNRs). Their bandwidths and gaps can be engineered by varying the size of the quantum dot and the neck width at indented edges. Effects of defects and contact junction on electrical conductance, Seebeck coefficient and electron thermal conductance of t-GNRs are calculated. When a defect occurs in the interior site of textured ZGNRs (t-ZGNRs), the maximum power factor within the central gap or near the band edges is found to be insensitive to the defect scattering. Furthermore, we found that SGQDs formed by t-ZGNRs have significantly better electrical power outputs than those of textured ANGRs due to the improved functional shape of the transmission coefficient in t-ZGNRs. With a proper design of contact the maximum power factor (figure of merit) of t-ZGNRs could reach 90% (95%) of the theoretical limit.

I. INTRODUCTION

Due to global warming, the Kyoto protocol aiming to reduce CO_2 emissions was proposed in 1997. Since then, renewable energies including solar, wind, rain, tides, and geothermal heat are topics of tremendous scientific interest [1]. Thermoelectric devices can be used as power generators and refrigerators. The electrical power based on thermoelectric effects is one of the most important type of green energies [1-6]. Because of the inherent physics of thermoelectric effect, thermoelectric devices can fully avoid CO_2 , hydrofluorocarbons, and perfluorocarbons emissions. In addition, thermoelectric devices can sustain long operation time and avoid mechanical noises.

Recently, energy harvesting applications in nanoscale systems have attracted considerable attention[7-12]. How to obtain the maximum thermoelectric efficiency of heat engines with optimized electrical power output has been a key issue [9-12]. To improve the performance of a heat engine it is preferable to have the electron transport in ballistic regime and phonon transport in the diffusive scattering regime. Therefore, a high-performance thermoelectric device needs to provide a channel length shorter than the electron mean free path (λ_e) but much longer than the phonon mean free path (λ_{ph}) in order to reduce the ratio of phonon thermal conductance (κ_{ph}) to electron thermal conductance (κ_e) [13]. It was pointed out in ref. [9] that a Carnot heat engine favors the electron transport in an energy range where the transmission coefficient has a steep change with respect to energy, e.g. with a square-form (SF). Up to now it remains unclear how to realize a SF transmission coefficient in realistic thermoelectric devices with a short channel length between thermal contacts, [14,11].

Considerable scientific efforts paved the way to answer such an intriguing problem. Hicks and Dresselhaus theoretically demonstrated that the thermoelectric performance can be significantly enhanced in one-dimensional (1D) nanowires due to the reduced phonon thermal conductance and the enhanced Seebeck coefficient (S) [2,3]. According to theoretical modeling, κ_{ph} of 1D silicon quantum dot (QD) superlattices can be reduced by one order of magnitude in comparison with 1D nanowires [7,8]. Due to limitations in technology the dot-size fluctuation in the 1D silicon quantum-dot (QD) arrays still remains a serious issue. [15,16]

The discovery of graphene in 2004 opened the door for realizing 1D nanowires with small cross-section to degrade κ_{ph} [17], since one can fabricate graphene nanoribbons (GNRs) with atomic precision via the bottom-up approach[18]. This approach has been successfully applied to build more complex systems, such as armchair GNRs with periodically corrugated edges, called as textured AGNRs (t-AGNRs) here.[19-25] The scanning tunneling microscopy (STM) spectra of serially-coupled graphene quantum dots (SGQDs) synthesized by t-AGNRs were reported experimentally [25]. Novel graphene-based electronic devices have also focused on AGNRs and t-AGNRs [26]. Recently, the existence of edge states with topological protection in textured zigzag GNRs (t-ZGNRs) has been demonstrated theoretically [27].

Several experimental studies of thermoelectric properties of graphene-related materials have been reported in recent years [28-34]. Nevertheless, there is a paucity of studies to consider the contact effect on thermoelectric properties of t-AGNRs and t-ZGNRs[35]. In this work, our goal is to optimize the transmission coefficient of t-GNRs with length shorter than λ_e , but larger than

λ_{ph} under different coupling strengths with the electrical contact. We found that minibands can be formed in these t-GNRs, while their energy gaps can be tuned by varying the size of GQDs and the inter-dot coupling strength. Furthermore, the calculated power factor is very robust against scattering from defects occurring inside the interior of these t-ZGNRs. The transmission coefficients through the minibands of t-ZGNRs under optimized tunneling rates provide desired characteristics showing steep change with respect to energy near the central gap that mimics the theoretical limit obtained by using a SF transmission coefficient. Due to this feature, our calculations reveal that the thermoelectric performance of t-ZGNRs can be significantly better than the t-AGNRs. The maximum power factor (figure of merit) of t-ZGNRs could reach 90% (95%) of that obtained with the SF transmission coefficient. Therefore, the t-ZGNR is a promising candidate for applications in nanoscale energy harvesting.

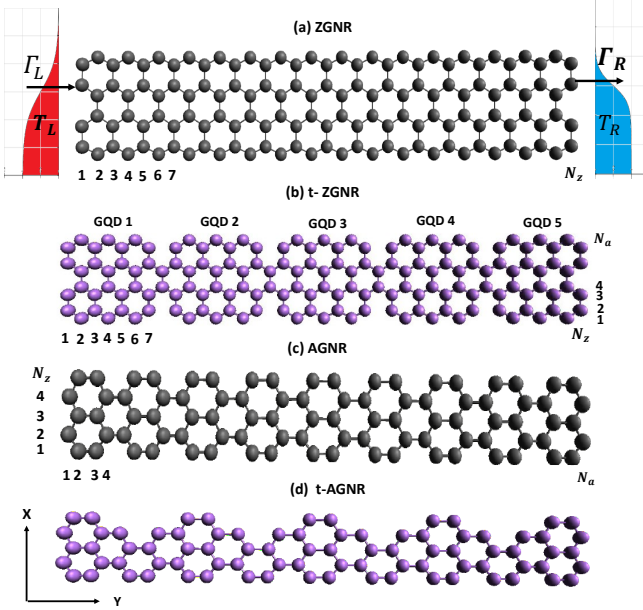


FIG. 1: Schematic diagrams of (a) ZGNR, (b) textured-ZGNR (t-ZGNR), (c) AGNR, and (d) t-AGNR. In (a), we also show the electrodes with Γ_L (Γ_R) denoting the tunneling rate of the electrons between the left (right) electrode and the leftmost (rightmost) atoms of the ZGNR. T_L and T_R denote the temperature of the left (L) and the right (R) electrodes, respectively. Note that t-ZGNRs can be formed by periodically removing some carbon atoms on the zigzag edges of ZGNRs. In (b) the t-ZGNR consists of GQDs with size characterized by $(N_a, N_z) = (8, 7)$. In (c) the AGNR has a length $N_a = 36$ and width $N_z = 5$. In (d), the width and length of the unit cell for the t-AGNR superlattice are characterized by $N_z = 5$ and $N_a = 8$, respectively.

II. CALCULATION METHOD

To model the thermoelectric properties of t-GNRs connected to the electrodes, it is a good approximation to employ a tight-binding model with one p_z orbital per atomic site to describe the electronic states.[36-40] The Hamiltonian of the nano-junction system depicted in Fig. 1, including four different GNR structures, can be written as $H = H_0 + H_{GNR}$ [41], where

$$H_0 = \sum_k \epsilon_k a_k^\dagger a_k + \sum_k \epsilon_k b_k^\dagger b_k \quad (1)$$

$$+ \sum_\ell \sum_k V_{k,\ell,j}^L d_{\ell,j}^\dagger a_k + \sum_\ell \sum_k V_{k,\ell,j}^R d_{\ell,j}^\dagger b_k + h.c.$$

The first two terms of Eq. (1) describe the free electrons in the left (L) and right (R) electrodes. a_k^\dagger (b_k^\dagger) creates an electron with wave number k and energy ϵ_k in the left (right) electrode. $V_{k,\ell,j=1}^L$ ($V_{k,\ell,j=N_z(N_a)}^R$) describes the coupling between the left (right) lead with its adjacent atom in the ℓ -th row.

$$H_{GNR} = \sum_{\ell,j} E_{\ell,j} d_{\ell,j}^\dagger d_{\ell,j} \quad (2)$$

$$- \sum_{\ell,j} \sum_{\ell',j'} t_{(\ell,j),(\ell',j')} d_{\ell,j}^\dagger d_{\ell',j'} + h.c.,$$

where $E_{\ell,j}$ is the on-site energy for the p_z orbital in the ℓ -th row and j -th column. Here, the spin-orbit interaction is neglected. $d_{\ell,j}^\dagger$ ($d_{\ell,j}$) creates (destroys) one electron at the atom site labeled by (ℓ,j) where ℓ and j , respectively are the row and column indices as illustrated in Fig. 1. $t_{(\ell,j),(\ell',j')}$ describes the electron hopping energy from site (ℓ,j) to site (ℓ',j') . The tight-binding parameters used for GNRs is $E_{\ell,j} = 0$ for the on-site energy and $t_{(\ell,j),(\ell',j')} = t_{pp\pi} = 2.7$ eV for nearest-neighbor hopping strength.

To study the transport properties of a GNR junction connected to electrodes, it is convenient to use the Keldysh Green's function technique [41]. Electron and heat currents leaving the electrodes can be expressed as

$$J = \frac{2e}{h} \int d\varepsilon \mathcal{T}_{LR}(\varepsilon) [f_L(\varepsilon) - f_R(\varepsilon)], \quad (3)$$

and

$$Q_{e,L(R)} = \frac{\pm 2}{h} \int d\varepsilon \mathcal{T}_{LR}(\varepsilon) (\varepsilon - \mu_{L(R)}) [f_L(\varepsilon) - f_R(\varepsilon)] \quad (4)$$

where $f_\alpha(\varepsilon) = 1/\{\exp[(\varepsilon - \mu_\alpha)/k_B T_\alpha] + 1\}$ denotes the Fermi distribution function for the α -th electrode, where μ_α and T_α are the chemical potential and the temperature of the α electrode. e , h , and k_B denote the electron charge, the Planck's constant, and the Boltzmann constant, respectively. $\mathcal{T}_{LR}(\varepsilon)$ denotes the transmission coefficient of a GNR connected to electrodes, which can be solved by the formula $\mathcal{T}_{LR}(\varepsilon) = 4Tr[\Gamma_L(\varepsilon)G^r(\varepsilon)\Gamma_R(\varepsilon)G^a(\varepsilon)]$ [42,43], where $\Gamma_L(\varepsilon)$ and $\Gamma_R(\varepsilon)$ denote the tunneling rate (in energy units) at the left and right leads, and $G^r(\varepsilon)$ and $G^a(\varepsilon)$ are the retarded

and advanced Green's functions of the GNR, respectively. The tunneling rates are described by the imaginary part of self-energy correction on the interface atoms of the GNR due to the coupling with nearby atoms in the adjacent electrodes, i.e. $\Gamma_{L(R)}(\varepsilon) = -Im(\Sigma_{L(R)}^r(\varepsilon))$. Such a coupling depends on the contact quality with the electrodes, which is characterized by the interaction strength $V_{k,\ell,j=1}^L (V_{k,\ell,j=N_z(N_a)}^R)$ with the left (right) lead. Here, we have adopted energy-independent tunneling rates $\Gamma_{L(R)}(\varepsilon) = \Gamma_{L(R)}$ which is reasonable in the wide-band limit for the electrodes [42]. Note that Γ_α and Green's functions are matrices in the basis of tight-binding orbitals. Γ_α for the boundary atoms have diagonal entries given by the same constant Γ_t . Because of the line contact as illustrated in Fig. 1, the contact resistance can be much smaller than that of surface contact [44]. Meanwhile, the variation of tunneling rates could reveal different contact properties such as the Schottky barrier or ohmic contact [45].

In the linear response regime, the electrical conductance (G_e), Seebeck coefficient (S) and electron thermal conductance (κ_e) are given by $G_e = e^2 \mathcal{L}_0$, $S = -\mathcal{L}_1/(eT\mathcal{L}_0)$ and $\kappa_e = \frac{1}{T}(\mathcal{L}_2 - \mathcal{L}_1^2/\mathcal{L}_0)$ with \mathcal{L}_n ($n = 0, 1, 2$) defined as

$$\mathcal{L}_n = \frac{2}{h} \int d\varepsilon \mathcal{T}_{LR}(\varepsilon) (\varepsilon - \mu)^n \frac{\partial f(\varepsilon)}{\partial \mu}. \quad (5)$$

Here $f(\varepsilon) = 1/(\exp^{(\varepsilon - \mu)/k_B T} + 1)$ is the Fermi distribution function of electrodes at equilibrium temperature T and chemical potential μ . As seen in Eq. (5), the transmission coefficient $\mathcal{T}_{LR}(\varepsilon)$ plays a significant role for electron transport between the left (L) and right (R) electrodes. At zero temperature, the electrical conductance is given by $G_e(\mu) = \frac{2e^2}{h} \mathcal{T}_{LR}(\mu)$. In the current study, only even numbers of N_a are considered to avoid unwanted dangling-bond states. We have developed an efficient computation method that allows us to calculate the Green's functions of large-sized quantum structures. For the current study, textured ZGNRs and AGNRs with lengths up to 14nm are considered.

III. RESULTS AND DISCUSSION

A. Graphene nanoribbons

Topological states offer promising applications in electronics and optoelectronics, owing to their robustness in transport characteristics against defect scattering. Many studies have confirmed that 2D and 1D topological states (TSs) exist in certain material structures [46-51]. For instance, there exists a 2D topologically protected interface state in HgTe/CdTe superlattices [46,47]. One-dimensional (1D) TSs were theoretically predicted to exist in square selenene and tellurene [51]. Recently, zero-dimensional (0D) TSs of finite-size GNRs have been extensively studied [19-25] because the 0D TS offers more

flexibility in the design of complicated electronic circuits [22]. Before illustrating electron coherent transport through SGQDs formed by t-ZGNRs, we first examine the characteristics of 0D TSs of finite-size GNRs by calculating their transmission coefficient, $\mathcal{T}_{LR}(\varepsilon)$.

Figure 2 shows the calculated electron conductance, G_e at $k_B T = 0$ as a function of μ for various N_a with $N_z = 7$. We note that there are two zigzag edge states localized at the top and bottom sides of the GQDs depicted in Fig. 1(a). For $N_a = 40$, their wave functions are well separated along the armchair direction [37]. The electrical conductance spectrum shows that $G_e = 2G_0$ at $\mu = 0$ and $G_e = G_0$ for other electronic states, where $G_0 = \frac{2e^2}{h}$ is the quantum conductance. Such zero energy modes were observed experimentally by STM [23]. When two electronic states are closely spaced (with energy separation less than the broadening), G_e can become large than G_0 . As N_a decreases, G_e for the zero-energy mode is split into two peaks corresponding to the bonding and antibonding states of coupled zigzag edge states, as seen in Fig. 2c. When $N_a = 12$, these two peaks are well separated. Here, ϵ_{HO} and ϵ_{LU} denote the energy levels of the highest occupied molecular orbital (HOMO) and the lowest unoccupied molecular orbital (LUMO), respectively. Due to the short decay lengths along the armchair edge directions for zigzag edges states, $\mathcal{T}_{LR}(\varepsilon)$ of Σ_0 also depends on whether the zigzag or armchair edges are coupled to the electrodes. In Ref. [52] it is proposed that a single QD can be used to realize a Carnot heat engine. However, the channel length for $N_z = 7$ ($L_z = 0.738$ nm) is too small to avoid the serious degradation of the figure of merit due to the phonon heat conductivity, κ_{ph} . On the other hand, for the large N_z case ($N_z \gg N_a$), a finite GNR shows metallic behavior, leading to unfavorable thermoelectric properties. To maintain a sizable gap ($10k_B T$) around the charge neutrality point (CNP) while keeping κ_{ph} small enough to preserve decent figure of merit ($ZT = \frac{S^2 G_e T}{\kappa_e + \kappa_{ph}}$), the t-ZGNR becomes a suitable candidate as we shall discuss below.

B. SGQDs formed by textured ZGNRs

For energy harvesting applications at room temperature, we need to design a $\mathcal{T}_{LR}(\varepsilon)$ spectrum with a square shape near the central gap to obtain optimized ZT and electrical power output [9]. Let's consider an SGQD formed by t-ZGNR. A t-ZGNR can be realized by tailoring GNR with periodic indentation on the zigzag edges such as the structure shown in Fig.1(b). This t-ZGNR consists of GQDs with size characterized by $N_a = 12$ and $N_z = 7$. A single GQD of this size has resonance energies $\epsilon_{LU(HO)} = \pm 0.247$ eV near the CNP, as shown in Fig. 2(c). For two coupled GQDs (2GQDs), there is one satellite peak on the left (right) side of the $\epsilon_{HO(LU)}$ peak (see Fig. 3(b)). For six coupled GQDs (6GQDs), we have five additional peaks with $\epsilon_{e(h),1} = \pm 0.3105$ eV, $\epsilon_{e(h),2} =$

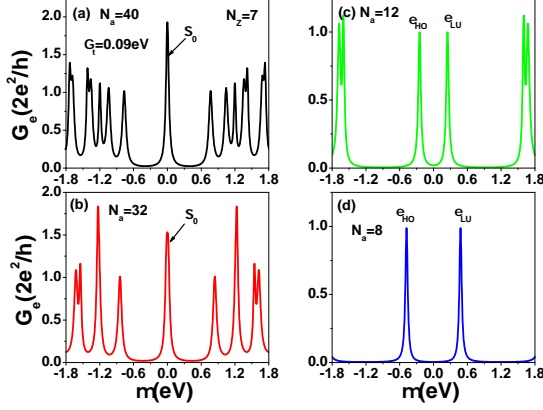


FIG. 2: Electrical conductance, G_e of a finite GNR with armchair edges coupled to the electrodes at $k_B T = 0$ as a function of the chemical potential, μ for various widths with $N_a = 40, 32, 12$, and 8 with N_z fixed at 7 . We have adopted electron tunneling rates $\Gamma_t = 90$ meV.

$\pm 0.468\text{eV}$, $\varepsilon_{e(h),3} = \pm 0.6705\text{eV}$, $\varepsilon_{e(h),4} = \pm 0.882\text{eV}$ and $\varepsilon_{e(h),5} = \pm 1.0665\text{eV}$ on the right (left) side of $\varepsilon_{LU(HO)} = \pm 0.247\text{eV}$ (see Fig. 3(f)). We note that $G_e(\mu)$ is fully suppressed for μ between ε_{HO} and ε_{LU} . Therefore, SGQDs formed by t-ZGNRs function as filters to block electrons with energies near the CNP, which is different from that of serially coupled antidots realized by ZGNRs with nanopores [53]. The separation between peaks is inhomogeneous. In addition, the ε_{HO} and ε_{LU} peaks become sharper with increasing GQD number. These features are attributed to a special parity symmetry in the supercell of ZGNRs. Due to the coupling of transverse and longitudinal wave numbers in ZGNRs, the density distributions of electronic state near CNP are inhomogeneous [54]. AGNRs do not have such a parity in the supercell. The feature provides a significant effect on the transmission coefficient of SGQDs formed by t-ZGNRs. To further illustrate the characteristics of the edge states we show the charge densities of states with ε_{LU} , $\varepsilon_{e,1}$ and $\varepsilon_{e,2}$ for the case of 6GQDs in Fig. A.1 of the appendix.

Previous theoretical studies have demonstrated that edge defects can significantly reduce the electron quantum conductance of ZGNRs [55,56]. Here, we investigate how defects (either at the edge or in the interior region) influence the thermoelectric characteristics of t-ZGNRs by introduce energy shifts $\Delta_{\ell,j}$ on designated defect sites. $\Delta_{\ell,j}$ could be positive or negative, which depends on the kind of defects [56]. To model a vacancy within a tight binding model, one typically takes $\Delta_{\ell,j} \rightarrow \infty$. The larger orbital-energy shift, the stronger effect on the electrical conductance can be seen [57]. Here, we consider the case of a positive and large Δ to investigate the effects of defects on the electron transport of t-ZGNRs. We calculate G_e , κ_e , S and power factor $PF = S^2 G_e$ for different defect locations for the case of 15 GQDs ($L_z = 14.5\text{nm}$ or

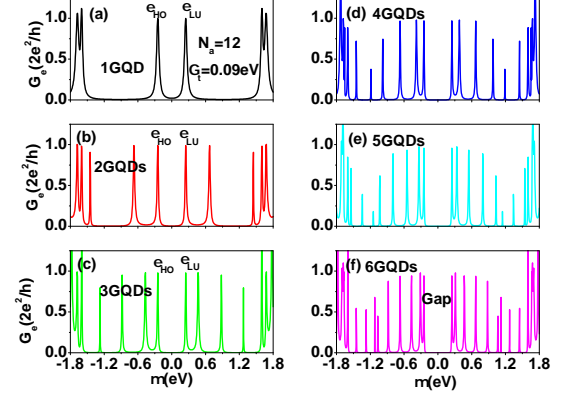


FIG. 3: Electrical conductance, G_e as a function of μ for SGQDs with various of GQD numbers. A SGQD consists of GQDs with the size characterized by $N_a = 12$ and $N_z = 7$. Other physical parameters correspond to those of Fig. 2(c).

$N_z = 119$) with $\Gamma_t = 0.54\text{eV}$ and show the results in Fig. 4.

As seen in Fig. 4(a) and 4(b), the size of the central gap and the shape of G_e and κ_e spectra (green lines) are changed only slightly when the defects are located in the interior region. However the G_e and κ_e values near the central gap become seriously suppressed (as shown by red lines) when a single defect is located at a zigzag edge site labeled by (1, 4), where the charge density of the $\varepsilon_{LU(HO)}$ electronic state is peaked. As seen in Fig. 4(c) the anti-symmetric pattern of the Seebeck coefficient $S(\mu)$ (with respect to the sign change of μ) due to the electron-hole symmetry is distorted in the presence of defects. The peak value of the power factor $PF = S^2 G_e$ near the central gap is seriously reduced when defects occur on the edge, but much less affected by defects in the interior region as illustrated in Fig. 4(d). Here and henceforth, κ_e is in units of $\kappa_0 = 0.62nW/K$, S is expressed in units of $k_B/e = 86.25\mu V/K$, and the power factor (PF) in units of $2k_B^2/h = 0.575pW/K^2$. It is remarkable to see that PF is very robust against defect scattering when defects are away from zigzag edges. Such location-dependent effects can be depicted by the charge density distribution in Fig. A1. To reduce defect effect on electron transport, one needs to avoid creating defects randomly located on the zigzag edges.

We note that SGQDs are formed by periodically removing some carbon atoms on the zigzag edges of ZGNRs. To understand the relationship between the quantum states near the central gap in the SGQD formed by t-ZGNRs and the quantum states near the zero energy modes of ZGNRs, we show a comparison of subband structures of the infinite long t-ZGNR shown in Fig. 1(b) and unaltered ZGNR shown in Fig. 1(a) (with an enlarged super cell of length $L = 4a$ to match the unit cell of t-ZGNR) in Fig. A.2(a) of the appendix. Note that

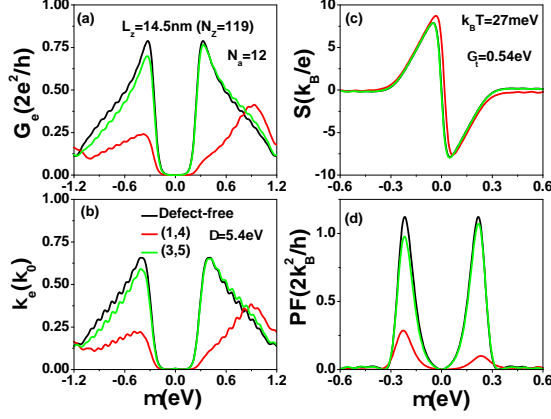


FIG. 4: (a) Electrical conductance G_e , (b) electron thermal conductance κ_e , (c) Seebeck coefficient S , and (d) power factor $PF = S^2 G_e$ as functions of μ for defect locations at $k_B T = 27 \text{ meV}$. The tunneling rates used are $\Gamma_t = 0.54 \text{ eV}$. The length of SGQD is $L_z = 14.5 \text{ nm}$ ($N_z = 119$). Each GQD in the SGQD structure has size $N_a = 12$ and $N_z = 7$.

the first Brillouin zone (BZ) has one quarter the size of the BZ of ZGNR. Thus, the subband structures shown in Fig. A.2(a) includes the zone-folding effect that maps the zone boundary ($k_z = \pi/a$) of the unfolded BZ of ZGNR to $k_z = 0$ of the folded BZ here. As expected, the unaltered ZGNR has edge states with zero energy for $k_z < 0.06\pi/a = 0.24\pi/L$. The two edge states are strongly coupled in the t-ZGNR with an energy splitting of 2.5 eV . On the other hand, the edge states at mini-zone boundary ($k_z = \pi/L$) with energies corresponding to the HOMO (LUMO) level are nearly unaffected by the removal of a carbon atom in the neck region of t-ZGNR, since the wave functions of these edge states have a node at that position. Theoretical calculations of the Zak phases of various t-ZGNRs indicate that the topological nature of edge states of t-ZGNRs are preserved even though their energy levels are shifted away from the CNP [27]. Thus, these states are topologically protected and the transport through these states should be rather insensitive to the presence of defects inside the t-ZGNR.

Junction tunneling rates can be affected by the quality of contact between the electrode and semiconductor,[44] which is a critical issue for device applications of two-dimensional materials.[58] To clarify the contact effect, we show in Fig. 5 the calculated G_e , κ_e , S , and ZT at room temperature for various tunneling rates (Γ_t) for a t-ZGNR with 15 GQDs, each having the dimension $N_a = 8$ and $N_z = 7$ as shown in Fig. 1(b). When the tunneling rate increases, the transmission coefficient $\mathcal{T}_{LR}(\epsilon)$ through minibands close to HOMO (LUMO) are enhanced. For the case of 15 GQDs, there are 15 peaks in each miniband (see Fig. A.3). Such an enhancement leads to an increase of both G_e and κ_e as seen in Fig. 5(a) and 5(b). However, S is essentially independent to

the variation of Γ_t as indicated by the collapsing of all four curves in Fig. 5(c). As a result, the power factor $PF = S^2 G_e$ also increases with Γ_t . It is noted that the maximum S reaches 1.51 mV/K [see Fig 5(c)], which is much larger than that observed experimentally in gapless graphene [28,29]. In Fig. 5(d), the maximum ZT occurs at $\mu = \pm 0.423 \text{ eV}$, where $\kappa_{ph} \gg \kappa_e$. Therefore, the enhancement of ZT with respect to the increase of Γ_t mainly arises from the enhancement of PF . Here, we have included the effect of phonon thermal conductance, κ_{ph} , and assumed $\kappa_{ph} = F_s \kappa_{ph}^0$ in the calculation of ZT in Fig. 5(d), where $\kappa_{ph}^0 = \frac{\pi^2 k_B^2 T}{3h}$ is the phonon thermal conductance of an ideal ZGNR. We adopt the room-temperature value of $\kappa_{ph}^0 = 0.285 \text{ nW/K}$ for ZGNR with width $N_a \leq 8$ obtained by a first-principles calculation as given in ref[59]. $F_s = 0.1$ denotes a reduction factor resulting from quantum constriction in t-ZGNRs. It has been theoretically demonstrated that the magnitude of κ_{ph} can be reduced by one order magnitude for ZGNRs with "edge vacancies" ref[60], which is similar to the mechanism introduced in silicon nanowires with surface roughness[61]. The measured λ_{ph} can be reduced from $300 - 600 \text{ nm}$ in a single layer graphene to 10 nm in graphene nanostructures (see [30] and references therein). Recently, very short λ_{ph} has been reported experimentally, which offers promise for enhancing the figure of merit (ZT) of graphene heterostructures[31-34].

The calculated results shown in Fig. 5 imply that $ZT > 3$ could be realized by using SGQDs formed by t-ZGNRs for tunneling rates corresponding to Γ_t between $t_{pp\pi}/10 = 0.27 \text{ eV}$ and $t_{pp\pi}/5 = 0.54 \text{ eV}$. In Fig. A.3 of the appendix, we show the peak value of ZT (ZT_{max}) as a function of tunneling rate Γ_t , and we found that the ZT_{max} can be larger than 3 for Γ_t between 0.18 eV and 1.45 eV . We note that if a semi-infinite ZGNR contact is used, it is reasonable to assume that the coupling strength between the semi-infinite ZGNR and t-ZGNR can be comparable to the hopping strength $t_{pp\pi} = 2.7 \text{ eV}$. Here, we show that the maximum ZT can reach 3.7 with $\Gamma_t = 0.54 \text{ eV} = t_{pp\pi}/5$ that could be achievable by a good contact.

Because S is a robust physical quantity with respect to the variation of tunneling rate and channel length (which only depend on the magnitude of central gap and temperature in our case), the optimization of G_e becomes a critical issue in SGQDs when $\kappa_{ph} \gg \kappa_e$. To provide better understanding of the effect of tunneling rate on thermoelectric properties, we further investigate the relation between tunneling rate and the spectral shape of $\mathcal{T}_{LR}(\epsilon)$. In Fig. 6, we show a comparison of the tunneling spectra, $\mathcal{T}_{LR}(\epsilon)$ of a t-ZGNR with 15 GQDs calculated for two different tunneling strengths $\Gamma_t = 0.54 \text{ eV}$ and $\Gamma_t = t_{pp\pi} = 2.7 \text{ eV}$. In Fig. 6(a) the area below the $\mathcal{T}_{LR}(\epsilon)$ curve shows a right-triangle shape that has a steep change with respect to ϵ on the side toward the central gap. In Fig. 6(b) (with $\Gamma_t = t_{pp\pi} = 2.7 \text{ eV}$) the electron tunneling probability through the electronic states near $\epsilon_{LU(HO)}$ is highly suppressed, leading to an arch-like

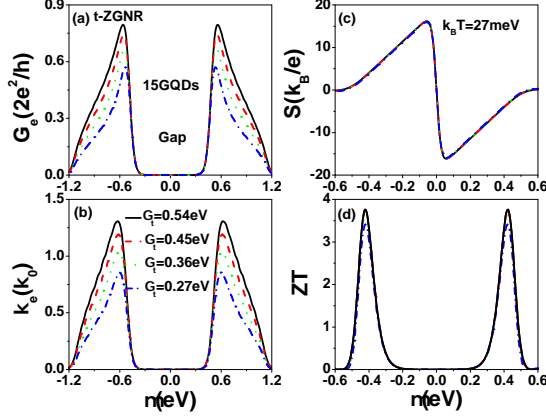


FIG. 5: (a) Electrical conductance G_e , (b) electron thermal conductance κ_e , (c) Seebeck coefficient S , and (d) figure of merit ZT as functions of μ for various tunneling rates (Γ_t) at $k_B T = 27 \text{ meV}$. The t-ZGNR structure with $L_z = 14.5 \text{ nm}$ considered is illustrated in Fig. 1(b). The size of each GQD in the t-ZGNR is characterized by $N_a = 8$ and $N_z = 7$.

area under the $\mathcal{T}_{LR}(\epsilon)$ curve. The corresponding maximum ZT for this case is 2.3, which is much smaller than that of Fig. 5(d). The results of Fig. 6(a) and Fig. 6(b) indicate that the shape of the area under $\mathcal{T}_{LR}(\epsilon)$ curve depends on the tunneling rate (or the quality of contact). An arch-like area under $\mathcal{T}_{LR}(\epsilon)$ will reduce the electrical conductance G_e near the central gap.

As seen in Fig. 6(c) the optimized PF found near $\Gamma_t = 0.54 \text{ eV}$ is very close to that obtained by using an ideal SF transmission spectrum (indicated by the red line), which exhibits the quantum limit of power factor for 1D systems with $PF_{QB} = 1.2659(\frac{2k_B^2}{h})$ [9,11]. We obtain the optimized $PF_{max} = 0.9PF_{QB}$, which is the same as that of the quantum interference heat engine [62]. This analysis suggests that using SGQDs with suitable tunneling rates could achieve the performance close to an optimum heat engine with maximum electrical power output and high thermoelectric efficiency. With the same κ_{ph} , ZT_{max} of t-ZGNRs can reach 95% of that obtained by a SF transmission coefficient (with $ZT_{max} = 3.951$). So far, we have only considered periodically indented structures on both the top and bottom zigzag edges (see Fig. 1(b)). We note that the same optimized result of $PF_{max} = 0.9PF_{QB}$ can also be achieved in periodically indented structures corresponding to Fig. 6 but with textured pattern only on one zigzag side provided that the tunneling rate can be increased to $\Gamma_t = 0.72 \text{ eV}$. The results are shown in Fig. A.3 in appendix.

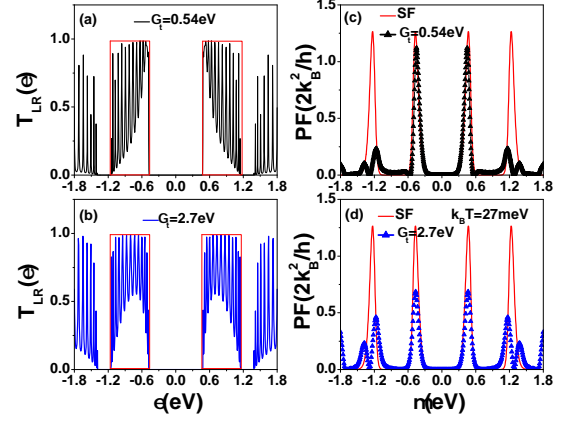


FIG. 6: (a) and (b) Transmission coefficients $\mathcal{T}_{LR}(\epsilon)$ as functions of energy for a t-ZGNR with $\Gamma_t = 0.54 \text{ eV}$ and $\Gamma_t = 2.7 \text{ eV}$. The $\mathcal{T}_{LR}(\epsilon)$ with square form (SF) is also plotted by a curve with red color. (c) and (d) Power factor as functions of μ for two tunneling rates at $k_B T = 27 \text{ meV}$. Other physical parameters are the same as those used in Fig. 5.

C. Armchair graphene nanoribbons

As shown in Figs. 5-6, SGQDs formed by metallic ZGNRs can become semiconductors. Next, we investigate whether its thermoelectric performance is better than that of AGNRs or t-AGNRs. We note that many designs have focused on the optimization of thermoelectric performance of AGNRs [63-66]. Here, we first consider AGNRs with their zigzag ends coupled to electrodes as depicted in Fig. 1(c). Figure 7 shows the calculated transmission coefficient $\mathcal{T}_{LR}(\epsilon)$ for different defect locations with $N_z = 7$, $N_a = 100$ and $\Delta = 5.4 \text{ eV}$. We choose $\Gamma_t = 2.7 \text{ eV}$, which gives the optimized shape of the transmission coefficient in defect free situation in Fig. 7(a). For finite-size AGNRs the conduction (valence) subband states are quantized, leading to closely-spaced peaks with staircase-like structures as revealed by the $\mathcal{T}_{LR}(\epsilon)$ spectrum. The area under $\mathcal{T}_{LR}(\epsilon)$ curve for states derived from the first subband has a parabolic shape, which does not meet the criterium for achieving optimized thermoelectric property. For a single defect at edge location (1,3), all but the transmission coefficient spectrum of the first conduction subband are affected significantly. When the defect is located at site (3,3), the spectra for the first conduction subband and the first valence subband are unaffected. Nevertheless, when the defect occurs at (4,4) the spectra in these two subbands show a remarkable change. In current studies we do not observe the Anderson localization effect, which leads to vanishing G_e in the subband regions when a single defect occurs on the edges of ZGNRs and AGNRs [67]. This implies that GNRs considered are not exact 1D systems.

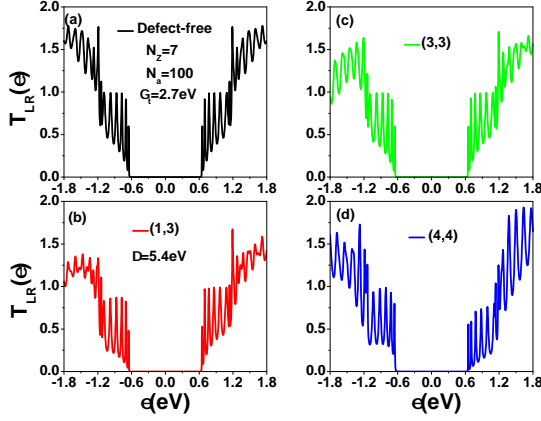


FIG. 7: Transmission coefficient of AGNRs as functions of ϵ for different defect locations at $\Gamma_t = 2.7\text{eV}$, $N_z = 7$ and $N_a = 100$ ($L_a = 10.5\text{nm}$). We have adopted $\Delta = 5.4\text{eV}$.

To illustrate the effects of defects on thermoelectric properties of finite AGNRs, we show the calculated electrical conductance (G_e), Seebeck coefficient (S), power factor (PF), and figure of merit (ZT) as functions of μ at $k_B T = 27\text{meV}$ in Fig. 8. Four curves in each diagram correspond to the effects of defects located at four sites considered in Fig. 7. As seen in Fig. 8a, the spectra of G_e for defects at locations (1,3) and (4,4) are degraded seriously either in the valence subband or conduction subband. Due to the robustness of the Seebeck coefficient in the central-gap region, the effect of defects on the power factor is solely determined by G_e . Although the maximum S is larger than that of Fig. 5(c) due to the larger gap in AGNRs with $N_z = 7$, the PF values are smaller than the corresponding values of the optimized t-ZGNR shown in Fig. 6 (with $\Gamma_t = 0.54\text{eV}$). This is mainly attributed to the different shapes in the area under the transmission-coefficient curve. As a consequence, the G_e resulting from thermionic tunneling effect is less favorable for AGNRs. Note that we have adopted $\kappa_{ph} = 0.0285\text{nW/K}$ in Fig. 8(d), which is the same as κ_{ph} in Fig. 5(d).

D. SGQDs formed by textured AGNRs

Finally, we study the thermoelectric effect of SGQD structures based on the t-AGNR structure as shown in Fig. 1d. The electronic structures and density of states (DOS) of t-AGNR superlattices have been studied theoretically by using density functional theory (DFT) [40,21]. Electronic structures of t-AGNRs can also be calculated by using a tight binding model and results are in good agreement with the DFT calculation[40]. Figure 9 shows the calculated $T_{LR}(\epsilon)$ of SGQD junctions made from t-AGNRs as functions of ϵ for three different N_a val-

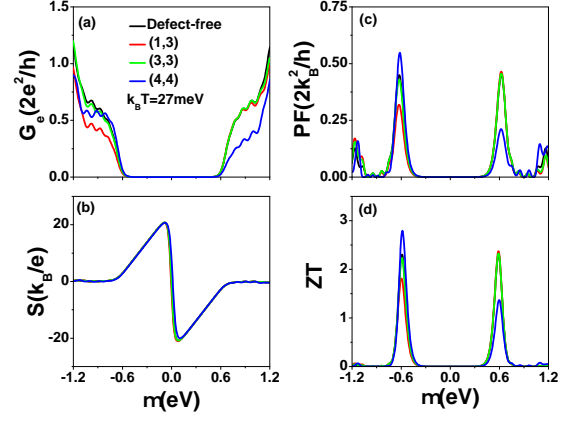


FIG. 8: (a) Electrical conductance G_e , (b) Seebeck coefficient S , (c) power factor PF and (d) figure of merit ZT as functions of μ for different defect locations at $k_B T = 27\text{meV}$. Other physical parameters are the same as those of Fig. 7. The considered $\kappa_{ph} = 0.0285\text{nW/K}$ is the same as that of Fig. 5 ($\kappa_{ph} = 0.0285\text{nW/K}$).

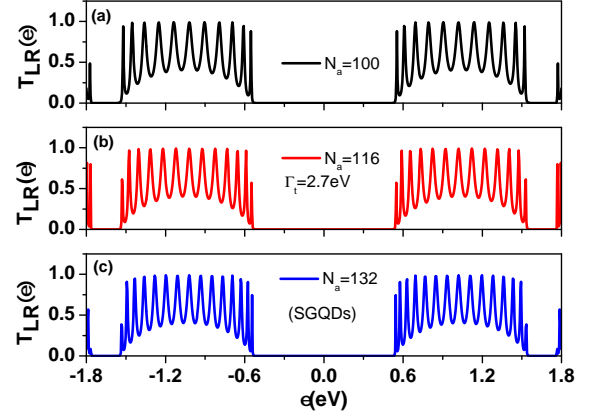


FIG. 9: Transmission coefficient of SGQD with $N_z = 5$ and various N_a values as functions of energy ϵ . $\Gamma_t = 2.7\text{eV}$. Here, $N_a = 12 + 8 \times N_{QD}$, where N_{QD} is the number of GQDs in the interior region of the structure, and they are sandwiched between two smaller GQDs of $N_a = 6$ connected to electrodes. Thus, $N_a = 100, 116$, and 132 correspond to $N_{QD} = 11, 13$, and 15 , respectively. For $N_a = 116$ and $N_a = 132$, the lengths of SGQDs are 12.2nm and 13.9nm , respectively.

ues with N_z fixed at 5. We adopt the optimized tunneling rate with $\Gamma_t = 2.7\text{eV}$. Although the AGNR with $N_z = 5$ is metallic, the textured AGNR can be semiconducting as illustrated by the sizable central gap (1.098eV) in Fig. 9. In Fig. A.2(b) of the appendix, we show a comparison of subband structures of the t-AGNR and unaltered AGNR (with an enlarged super cell of length $L = 2a'$ to match the unit cell of t-AGNR), where $a' = \sqrt{3}a$ is the unit

cell length of AGNR. We see that the two subbands with linear dispersion in the metallic $N_z = 5$ AGNR are split into two subbands with parabolic dispersion near zero wave-number once the quantum constriction takes effect in the t-AGNR. It is worth noting that edge states with zero energy can exist at the left and right ends (with zigzag edges) of the truncated t-AGNR in contact with electrodes. These edge states can contribute to $\mathcal{T}_{LR}(\varepsilon)$ for t-AGNRs with short SGQD structure (see Fig. A.4 in appendix), since their wave functions decay exponentially along the armchair direction. The area under the $\mathcal{T}_{LR}(\varepsilon)$ curve has an arch-like shape that does not change much as we vary the tunneling rate.

Figure 10 shows the calculated G_e , S , PF and ZT of SGQD junctions made from a t-AGNR with $N_z = 5$ and $N_a = 132$ ($N_{QD} = 15$) as functions of temperature for different μ values. Solid and dashed lines correspond to $\mu = 0.52\text{eV}$ and $\mu = 0.36\text{eV}$, respectively. The first conduction subband edge occurs at $\mu_{edge} = 0.544\text{eV}$. At a given temperature $k_B T = 27\text{meV}$, the maximum power factor occurs at $\mu = 0.52\text{eV}$. For $\mu = 0.36\text{eV}$, which is far away from μ_{edge} , the calculated G_e in the thermionic assisted tunneling process (TATP) is extremely small, whereas its Seebeck coefficient is highly enhanced. The temperature-dependent S for this case is complicated. Its temperature dependence can be described by three different functions at three temperature ranges as illustrated in Fig. 10(b). In region one ($T < 90\text{K}$), we have $S_1 = -\frac{\pi^2 k_B^2 T}{3e} \frac{\partial \ln(\mathcal{T}_{LR}(\varepsilon))}{\partial \varepsilon} \big|_{\varepsilon=\mu}$. In region three ($T > 120\text{K}$) we have $S_3 = \frac{\mu - \mu_{edge}}{eT}$ [68]. In region 2, the analytic expression of S_2 is unknown. In TATP, G_e can be described by the expression $\exp(\mu - \mu_{edge})/(k_B T)$. As a consequence, the power factor and figure of merit are small for $\mu = 0.36\text{eV}$. When $\mu = 0.52\text{eV}$, the PF is enhanced quickly in the range $50\text{K} < T < 120\text{K}$. Within this temperature region, ZT shows a similar behavior of PF . When $T > 120\text{K}$, the temperature-dependent ZT has the same trend of S because the heat current is dominated by the linear- T phonon thermal conductance $\kappa_{ph} = F_s \frac{\pi^2 k_B^2 T}{3h}$, which cancels the factor of TG_e in the numerator of ZT . It is worth noting that the optimized PF of t-AGNRs at $T = 325\text{K}$ is only one-half of the power factor of the t-ZGNR shown in Fig. 6(c).

Overall, we found no appreciable improvement in the power factor of t-AGNRs in comparison to AGNRs. Although electron Coulomb interactions are neglected in this calculation, our conclusion is still valid even in the Coulomb blockade regime. When the thermoelectric behavior of SGQDs is dominated by the TATP, electron-electron correlation functions are usually small [69]. Therefore, we can neglect electron Coulomb interactions when μ is inside the gap between two subbands.

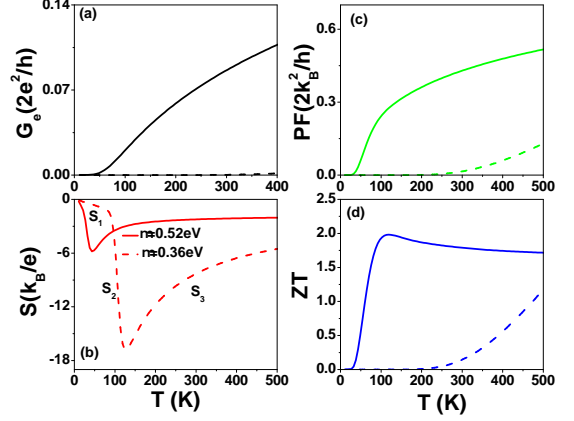


FIG. 10: (a) Electrical conductance G_e , (b) Seebeck coefficient S , (c) power factor PF and (d) figure of merit ZT of SGQD with $N_z = 5$ and $N_a = 132$ ($N_{QD} = 15$) as functions of temperature for different μ at $\Gamma_t = 2.7\text{eV}$. The phonon thermal conductance, κ_{ph} adopted is the same as in Fig. 8.

IV. CONCLUSION

We have theoretically investigated the transport and thermoelectric properties of SGQDs, which are formed by tailoring ZGNRs and AGNRs. Our calculations are based on the Green's function approach within a tight-binding model. Electron coherent tunneling process is found responsible for the electrical conductance spectra of SGQDs. Subband width and central gap of SGQDs can be modulated by varying the size of QDs and inter-dot coupling strength. Unlike G_e and κ_e , Seebeck coefficients are found insensitive to the contact property between the SGQDs and electrodes. As a result, the power factor and thermoelectric figure of merit can be improved by modulating the tunneling rates. The maximum ZT values at room temperature occur when the chemical potential, μ is close to the HOMO (LUMO) level in typical situation where phonon carriers dominate the heat transport. As shown in Fig. 6 and Fig. A.3, the maximum power factor (figure of merit) of t-ZGNRs at room temperature can reach 90 % (95 %) of the ideal situation with a square-form transmission coefficient. We also found that SGQDs based on t-ZGNRs can outperform SGQDs based on t-AGNRs for thermoelectric application. The significantly improved thermoelectric behavior of the textured ZGNR is attributed to the sharp change of its transmission coefficient near the central gap. We found that defects at interior sites will not ruin the robust behavior of $\mathcal{T}_{LR}(\varepsilon)$ associated with the edge states near LUMO of t-ZGNRs. It implies that the electron mean free path, λ_e contributed from the zigzag edge states ($\lambda_{e,edge}$) can be much larger than the contribution from bulk states ($\lambda_{e,bulk}$). When the channel length (L_z) of t-ZGNRs is much larger than λ_{ph} and $\lambda_{e,bulk}$, κ_{ph} is se-

riously suppressed in such a diffusing region. The electronic states in the first miniband (near LUMO) of t-ZGNRs showing nonlinear dispersion could remain coherent due to their unique nature [27]. As a consequence, the power factor of Fig. 6 remains valid, meanwhile the corresponding ZT could be further enhanced.[13] At room temperature with $T = 324K$ ($k_B T = 27meV$), the electrical power output can reach $0.212nW/K$ for each SGQD implemented by using t-ZGNR. For an SGQD array with density of $5 \times 10^6 cm^{-1}$ and ZT larger than 3, the estimated power output is around mW/K , which can be applicable for low-power wearable electronic devices[70].

Author contributions

David M T Kuo initiated the idea and performed the calculation.; David M T Kuo and Y. C. Chang both contributed to the development of the computation code and carried out the data analyses. David M. T. Kuo and Y. C. Chang wrote the manuscript. All authors read and agreed to the published version of the manuscript

Funding

This research was funded by the Ministry of Science and Technology Grant Number MOST 110-2112-M-001-042 and 110-2119-M-008-006-MBK in Taiwan

Data availability

The data presented in this study are available upon reasonable request.

Acknowledgments

This work was supported in part by the Ministry of Science and Technology (MOST), Taiwan under Contract Nos. 110-2112-M-001-042 and 110-2119-M-008-006-MBK.

Conflicts of interest

The authors declare no conflict of interest.

Appendix A

1. Charge density of t-ZGNRs

To further clarify the electronic states shown in Fig. 3, we plot the charge densities of $|\Psi_{\ell,j}(\varepsilon_{LU})|^2$, $|\Psi_{\ell,j}(\varepsilon_{e,1})|^2$ and $|\Psi_{\ell,j}(\varepsilon_{e,2})|^2$ for the 6-GQDs case formed by t-ZGNRs with $N_a = 12$ and $N_z = 47$ in Fig. A.1, which correspond to the electronic states of $\varepsilon_{LU} = 0.247eV$, $\varepsilon_{e,1} = 0.3105eV$ and $\varepsilon_{e,2} = 0.468eV$ in Fig. 3(f). As seen in Fig. A.1(a), the charge density distribution in each GQD is the same for the electronic state of ε_{LU} . The maximum charge densities appearing at bottom and top zigzag edge sites are contributed by $\ell = 1$ and $\ell = 12$ with the condition $j - 4 = 8m$, where m is an integer. At interior sites of each GQD the charge density is very low. For $\varepsilon_{e,1} = 0.3105eV$, the charge density at the central two GQDs is negligible. For $\varepsilon_{e,2} = 0.468eV$, the charge density at the 2nd and 5th GQDs are dilute. For $\varepsilon_{e,6} = 1.0665eV$, the charge density at the 1st and the 6th GQDs is smaller than those of other GQDs (not shown here). This indicates that the electronic states near $\varepsilon_{e,6} = 1.0665eV$ are weakly coupled to the elec-

trodes. Based on the charge density distribution shown in Fig. A.1, the defect location-dependent behavior of G_e shown in Fig. 4 can be clearly illustrated. The G_e does not be degraded seriously when defects locate at sites with low charge density.

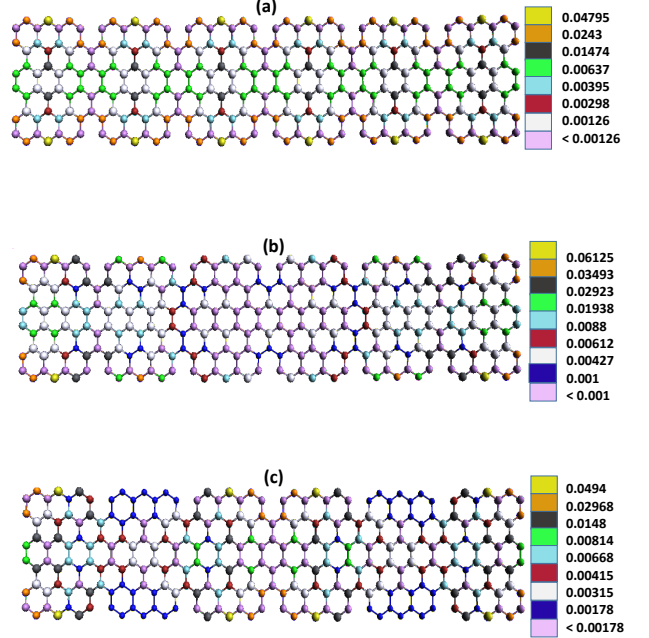


FIG. A.1: Charge density $|\Psi_{\ell,j}(\varepsilon)|^2$ for the t-ZGNR with conductance spectrum shown in Fig. 3(f). Diagrams (a), (b) and (c) are the charge densities of $\varepsilon_{LU} = 0.247eV$, $\varepsilon_{e,1} = 0.3105eV$, and $\varepsilon_{e,2} = 0.468eV$, respectively.

2. Electronic band structures

In Fig. A.2, we show comparisons of subband structures of graphene nanoribbons with and without modification of side edges. Here, the length of unit cell in t-GNRs is denoted L . For the t-ZGNR with its unit cell characterized by $N_a = 8$ and $N_z = 8$, we have $L = 4a$, where a is lattice constant of ZGNR. For the t-AGNR characterized by $N_z = 5$ and $N_a = 8$, we have $L = 2a'$, where $a' = \sqrt{3}a$ is the lattice constant of AGNR. We note that the first Brillouin zone (BZ) has one quarter (half) the size of the BZ of ZGNR (AGNR). Thus, the subband structures shown in Fig. A.1 includes the zone-folding effect that maps the zone boundary $k_z = \pi/a$ ($k_z = \pi/a'$) of the unfolded BZ of ZGNR (AGNR) to $k_z = 0$ of the folded BZ here. Here, we show the electronic structure of $N_a = 8$ rather than $N_a = 12$ in Fig. A.2(a). For $N_a = 8$, we observe not only the central gap, but also the gap between the first subband and the second subband.

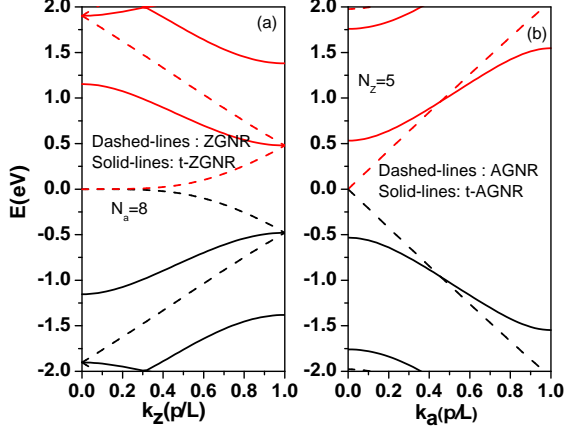


FIG. A.2: (a) Subband structures of t-ZGNR superlattice with a unit cell of length L characterized by $N_a = 8$ and $N_z = 8$ (solid lines) as depicted in Fig. 1(b), and corresponding ZGNR (without texture) of the same length of unit cell (dashed lines). (b) Subband structures of t-AGNR superlattice with a unit cell characterized by $N_z = 5$ and $N_a = 8$ (solid lines) as depicted in Fig. 1(d), and corresponding AGNR (without texture) of the same length of unit cell (dashed lines).

3. ZT optimization of textured ZGNRs

In Fig. A3, we show the calculated $\mathcal{T}_{LR}(\varepsilon)$ in the region of $\varepsilon > 0$ for two kinds of t-ZGNRs: (a) with indentation on both zigzag sides and (b) with indentation on only one zigzag side of the t-ZGNR. Both t-ZGNRs consist of 15 GQDs (same as the one considered in Figs. 5 and 6). The solid, dashed, dotted and dot-dashed lines correspond to $\Gamma_t = 0.45, 0.54, 0.63$ and 0.72 eV, respectively. As energy ε is tuned away from LUMO, many sharp peaks appear in the spectrum as a consequence of the Fabry-Perot interference. The period of Fabry-Perot interference in (b) is larger than that in (a). When ε gets close to LUMO, electronic states can not be clearly resolved due to their nonlinear dispersion. Diagram (c) shows ZT_{max} of a t-ZGNR consisting of 15 GQDs as a function of the tunneling rate Γ_t at $k_B T = 27$ meV and $\mu = 0.423$ eV. It is found that ZT_{max} can be larger than 3 for Γ_t between 0.18 eV and 1.45 eV for the case of (a). When the barrier height gets smaller, the miniband width becomes wider. This indicates that electron interdot hopping strengths are enhanced. That is why ZT_{max} occurs at $\Gamma_t = 0.72$ eV in (b). Since the theoretical limit for an ideal SF transmission coefficient is $ZT_{max} = 3.95167$, the maximum ZT value of t-ZGNRs can reach 95% of the ideal case.

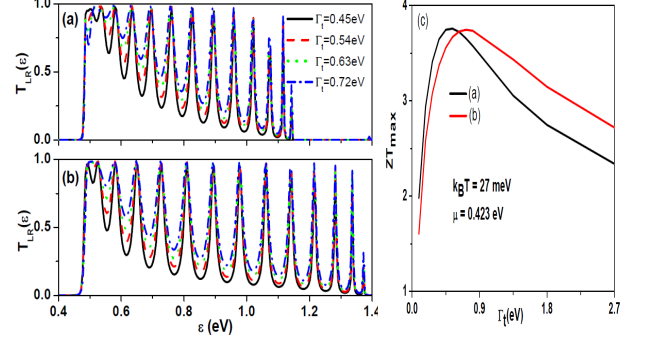


FIG. A.3: Transmission coefficient in the range of $\varepsilon > 0$ for different tunneling rates. (a) periodically indented structures on both zigzag-edge sides and (b) periodically indented structures on only one zigzag-edge side. (c) ZT_{max} of a t-ZGNR consisting of 15 GQDs as a function of the tunneling rate Γ_t . Each GQD in the structure has size $N_a = 8$ and $N_z = 7$. The maximum ZT value of SF transmission coefficient at $k_B T = 27$ meV is 3.95167 when its κ_{ph} is adopted the same as that of Fig. 5.

4. Local density of states of textured AGNRs

The $\mathcal{T}_{LR}(\varepsilon)$ spectrum cannot reveal the existence of zigzag edge states in a finite-size AGNR that decay exponentially along the armchair directions when the channel length is much longer than the decay lengths. These localized states of GNRs can be probed by STM [21]. In Fig. A.4, we show the calculated local density of states (LDOS) as a function of ε for various tunneling rates. Here, we define $LDOS = -Im(G_{\ell=2,j=1}^r(\varepsilon))/\pi$. The LDOS can reveal the existence of the zigzag edge states of an AGNR coupled to the electrodes. The zero energy modes resulting from the outer zigzag edge structures of t-AGNRs are seen in Fig. A.4. Due to the localized nature of the zigzag edge states, the spectra in Fig. 9 can not reveal them. Meanwhile, these edge state localized at the interface are also strongly influenced by the variation of coupling strength between the electrodes and the t-AGNR. With increasing Γ_t , these zero energy modes become broadened in (b) and (c).

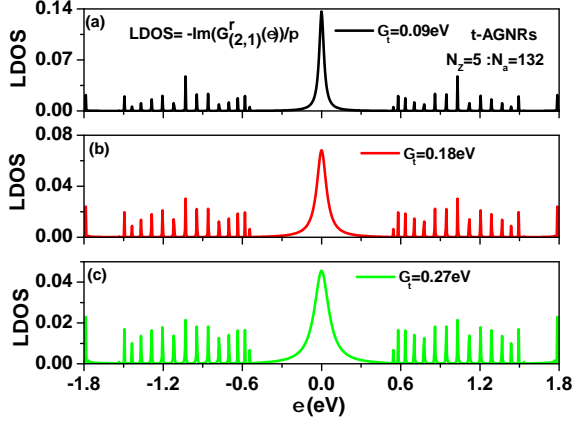


FIG. A.4: Local density of states of a t-AGNR with $(N_z, N_a) = (5, 132)$ as a function of ε for various tunneling rates at site $(2,1)$.

- ¹ G. Chen, M. S. Dresselhaus, G. Dresselhaus, J. P. Fleurial, and T. Caillat, *International Materials Reviews*, **48**, 45 (2003).
- ² L. D. Hicks and M. S. Dresselhaus, *Phys. Rev. B* **47**, 16631 (1993).
- ³ L. D. Hicks and M. S. Dresselhaus, *Phys. Rev. B* **47**, 12727 (1993).
- ⁴ A. Boukai, Y. Bunimovich, J. Tahir-Kheli, J.-K. Yu, W. A. Goddard III, and J. R. Heath, *Nature* **451**, 168 (2008).
- ⁵ A. Hochbaum, A. I. Hochbaum, R. Chen, R. D. Delgado, W. Liang, E. C. Garnett, M. Najarian, A. Majumdar, and P. D. Yang, *Nature* **451**, 163 (2008).
- ⁶ J. P. Heremans, C. M. Thrush, D. T. Morelli, and M. C. Wu, *Phys. Rev. Lett.* **88**, 216801 (2002).
- ⁷ D. L. Nika, E. P. Pokatilov, A. A. Balandin, V. M. Fomin, A. Rastelli, and O. G. Schmidt, *Phys. Rev. B* **84**, 165415 (2011).
- ⁸ M. Hu and D. Poulikakos, *Nano Lett.* **12**, 5487 (2012).
- ⁹ R. S. Whitney, *Phys. Rev. Lett.* **112**, 130601 (2014).
- ¹⁰ P. Pietzonka and U. Seifert, *Phys. Rev. Lett.* **120**, 190602 (2018).
- ¹¹ I. J. Chen, A. Burke, A. Svilans, H. Linke, and C. Thelander, *Phys. Rev. Lett.* **120**, 177703 (2018).
- ¹² R. Luo, G. Benenti, G. Casati, and J. Wang, *Phys. Rev. Lett.* **121**, 080602 (2018).
- ¹³ Y. Xu, Z. Gan, and S. C. Zhang, *Phys. Rev. Lett.* **112**, 226801 (2014).
- ¹⁴ P. Darancet, V. Olevano, and D. Mayou, *Phys. Rev. Lett.* **102**, 136803 (2009).
- ¹⁵ C. R. Kagan and C. B. Murry, *Nature Nanotechnology* **10**, 1013 (2015).
- ¹⁶ W. I. L. Lawrie et al, *Appl. Phys. Lett.* **116**, 080501 (2020).
- ¹⁷ K. S. Novoselov, A. K. Geim, S. V. Morozov, D. Jiang, Y. Zhang, S. V. Dubonos, I. V. Grigorieva, and A. A. Firsov, *Science* **306**, 666 (2004).
- ¹⁸ J. Cai, P. Ruffieux, R. Jaafar, M. Bieri, T. Braun, S. Blankenburg, M. Muoth, A. P. Seitsonen, M. Saleh, X. Feng, K. Mullen, and R. Fasel, *Nature* **466**, 470 (2010).
- ¹⁹ Y. C. Chen, T. Cao, C. Chen, Z. Pedramraz, D. Haberer, D. G. de Oteyza, F. R. Fischer, S. G. Louie and M. F. Crommie, *Nature Nanotechnology* **10**, 156 (2015).
- ²⁰ O. Groning, S. Wang, X. Yao, C. A. Pignedoli, G. B. Barin, C. Daniels, A. Cupo, V. Meunier, X. Feng, A. Narita, et al., *Nature* **560**, 209 (2018).
- ²¹ D. J. Rizzo, G. Veber, T. Cao, C. Bronner, T. Chen, F. Zhao, H. Rodriguez, S. G. Louie, M. F. Crommie, and F. R. Fischer, *Nature* **560**, 204 (2018).
- ²² L. H. Yan and P. Liljeroth, *ADVANCES IN PHYSICS: X* **4**, 1651672 (2019).
- ²³ D. J. Rizzo, G. Veber³, J. W. Jiang, R. McCurdy, T. Cao C. Bronner, T. Chen, Steven G. Louie¹, F. R. Fischer, M. F. Crommie, *Science* **369**, 1597 (2020).
- ²⁴ Q. Sun, Y. Yan, X. L. Yao, K. Mullen, A. Narita, R. Fasel, and P. Ruffieux, *J. Phys. Chem. Lett.* **12**, 8679 (2021).
- ²⁵ D. J. Rizzo, J. W. Jiang, D. Joshi, G. Veber, C. Bronner, R. A. Durr, P. H. Jacobse, T. Cao, A. Kalayjian, H. Rodriguez, P. Butler, T. Chen, Steven G. Louie, F. R. Fischer, and M. F. Crommie, *ACS Nano* **15**, 20633 (2021).
- ²⁶ J. P. Llinas et al, *Nature communications* **8**, 633 (2017).
- ²⁷ K. S. Lin and M. Y. Chou, *Nano Lett.* **18**, 7254 (2018).
- ²⁸ Y. M. Zuev, W. Chang, and P. Kim, *Phys. Rev. Lett.* **102**, 096807 (2009).
- ²⁹ P. Wei, W. Z. Bao, Y. Pu, C. N. Lau, and J. Shi, *Phys. Rev. Lett.* **102**, 166808 (2009).
- ³⁰ Y. Xu, Z. Y. Li, and W. H. Duan, *Small* **10**, 2182 (2014).
- ³¹ Y. H. Wang, J. Yang, L. Y. Wang, K. Du, Q. Yin, and Q. J. Yin, *ACS Appl. Mater. Interfaces* **9**, 20124 (2017).
- ³² M. Li, D. L. Cortie, J. X. Liu, D. H. Yu, SMKN Islam, L. L. Zhao, DRG Mitchell, R. A. Mole, M. B. Cortie, and S. X. Dou, *Nano energy* **53**, 993 (2018).

- ³³ S. Ghosh, S. Harish, M. Ohtaki, and B. B. Saha, *Material today energy*, **18**, 100492 (2020).
- ³⁴ Y. Y. Wang, D. R. Chen, J. K. Wu, T. H. Wang, C. S. Chuang, S. Y. Huang, W. P. Hsieh, M. Hofmann, Y. H. Chang, and Y. P. Hsieh, *Nano Lett.* **21**, 6990 (2021).
- ³⁵ Jian He and Terry M. Tritt, *Science* **357**, 1369 (2017).
- ³⁶ K. Nakada, M. Fujita, G. Dresselhaus, and M. S. Dresselhaus, *Phys. Rev. B* **54**, 17954 (1996).
- ³⁷ K. Wakabayashi, M. Fujita, H. Ajiki, and M. Sigrist, *Phys. Rev. B* **59**, 8271 (1999).
- ³⁸ Y. W. Son, M. L. Cohen, and Steven G. Louie, *Nature* **444**, 347 (2006).
- ³⁹ M. Topsakal, H. Sevincli, and S. Ciraci, *Appl. Phys. Lett.* **92**, 173118 (2008).
- ⁴⁰ H. Sevincli, M. Topsakal, and S. Ciraci, *Phys. Rev. B* **78**, 245402 (2008).
- ⁴¹ H. Haug and A. P. Jauho, *Quantum Kinetics in Transport and Optics of Semiconductors* (Springer, Heidelberg, 1996).
- ⁴² D. M. T. Kuo, *AIP Advances* **10**, 045222 (2020).
- ⁴³ T. T. Phung, R. Peters, A. Honecker, G. Trambly de Laisardiere, and J. Vahedi, *Phys. Rev. B* **102**, 035160 (2020).
- ⁴⁴ R. S. Chen, G. L. Ding, Y. Zhou, and S. T. Han, *J. Materials Chemistry C*, **9** 11407 (2021).
- ⁴⁵ G. D. Mahan and L. M. Woods, *Phys. Rev. Lett.* **80**, 4016 (1998).
- ⁴⁶ Y. C. Chang, J. N. Schulman, G. Bastard, and Y. Guldner, *Phys. Rev. B* **31**, 2557 (R) (1985).
- ⁴⁷ B. A. Bernevig, T. L. Hughes, and S. C. Zhang, *Science* **314**, 1757 (2006).
- ⁴⁸ L. Z. Kou, S. C. Wu, C. Felser, T. Frauenheim, C. F. Chen, and B. H. Yan, *ACS NANO* **8**, 10448-10454 (2014).
- ⁴⁹ H. Q. Huang and W. H. Duan, *Nature Materials* **15**, 129 (2016).
- ⁵⁰ Z. L. Zhu, X. L. Cai, S. H. Yi, L. Chen, Y. W. Dai, C. Y. Niu, Z. X. Guo, M. H. Xie, F. Liu, J. H. Cho, Y. Jia, and Z. Y. Zhang, *Phys. Rev. Lett.* **119**, 106101 (2017).
- ⁵¹ L. Xian, A. PerezPaz, E. Bianco, P. M. Ajayan and A. Rubio, *2D materials*. **4**, 041003 (2017).
- ⁵² G. D. Mahan and J. O. Sofo, *Proc. Natl. Acad. Sci. USA* **93**, 7436 (1996).
- ⁵³ P. H. Chang, M. S. Bahramy, N. Nagaosa, and B. K. Nikolic, *Nano Lett.* **14**, 3779 (2014).
- ⁵⁴ K. Wakabayashi, K. Sasaki, T. Nakanishi, and T. Enoki, *Sci. Technol. Adv. Mater.* **11** 054504 (2010).
- ⁵⁵ D. A. Areshkin, Daniel Gunlycke, and C. T. White, *Nano Lett.* **7**, 204 (2007).
- ⁵⁶ T. B. Martins, Antonio J. R. da Silva, R. H. Miwa and A. Fazzio, *Nano Lett.* **8**, 2293 (2008).
- ⁵⁷ T. C. Li and Shao-Ping Lu, *Phys. Rev. B* **77**, 085408 (2008).
- ⁵⁸ P. C. Shen et al, *Nature* **593**, 212 (2021).
- ⁵⁹ H. Zheng, H. J. Liu, X. J. Tan, H. Y. Lv, L. Pan, J. Shi, and X. F. Tang, *Appl. Phys. Lett.* **100**, 093104 (2012).
- ⁶⁰ H. Sevincli and G. Cuniberti, *Phys. Rev. B* **81**, 113401 (2010).
- ⁶¹ P. G. Murphy and J. E. Moore, *Phys. Rev. B* **76**, 155313 (2007).
- ⁶² P. Samuelsson, S. Kheradsoud, and B. Sothmann, *Phys. Rev. Lett.* **118**, 256801 (2017).
- ⁶³ F. Mazzamuto, V. Hung Nguyen, Y. Apertet, C. Caer, C. Chassat, J. Saint-Martin, and P. Dollfus, *Phys. Rev. B* **83**, 235426 (2011).
- ⁶⁴ P. Dollfus, V. H. Nguyen, and J. Saint-Martin, *J. Phys: Condens. Matter* **27**, 133204 (2015).
- ⁶⁵ V. T. Tran, J. Saint-Martin, and P. Dollfus, *Nanotechnology* **26**, 495202 (2015).
- ⁶⁶ N. Merino-Diez, A. Garcia-Lekue, E. Carbonell-Sanroma, J. C. Li, M. Corso, L. Colazzo, F. Sedona, D. Sanchez-Portal, J. I. Pascual, and D. G. de Oteyza, *ACS NANO*, **11**, 11661 (2017).
- ⁶⁷ P. A. Lee and T. V. Ramakrishnan, *Rev. Mod. Phys.* **57**, 287 (1985).
- ⁶⁸ D. M.-T. Kuo and Y. C. Chang, *Phys. Rev. B* **81**, 205321 (2010).
- ⁶⁹ D. M. T. Kuo, C. C. Chen, and Y. C. Chang, *Phys. Rev. B* **95**, 075432 (2017).
- ⁷⁰ F. Suarez, A. Nozariasbmaz, D. Vashae, and M. C. Ozturk, *Energy Environ Sci*, **9**, 2099 (2016).